Surface oxygen vacancy induced α-MnO$_2$ nanofiber for highly efficient ozone elimination

Guoxiang Zhu [a], Jinguo Zhu [b], Wenjun Jiang [a], Zijian Zhang [a], Jun Wang [a], Yongfa Zhu [a,*], Qianfan Zhang [b,*]

[a] Department of Chemistry, Tsinghua University, Beijing 100084, China
[b] School of Materials Science and Engineering, Beihang University, Beijing 100191, China

ARTICLE INFO

ABSTRACT

α-MnO$_2$ nanofiber with high concentration of surface oxygen vacancy was obtained via vacuum deoxidation method. The activity of α-MnO$_2$ strongly depends on the concentration and extent of oxygen vacancy, which can be adjusted by tuning the temperature and time of vacuum deoxidation. The formation of oxygen vacancy enhanced the ratio of Mn^{3+}/Mn^{4+}, which changed the charge distribution on the α-MnO$_2$ nanofiber, resulting in a significant improvement of the adsorption of ozone on the surface of the catalyst. In the dry gas flow, the ozone removal rate at 20 h has increased from 32.6% to 95%. In the wet gas flow, the ozone removal rate was also enhanced thanks to more active sites offered by α-MnO$_2$. What's more, we found that the deactivation caused by water vapor was temporary and the activity would recover once the humidity has decreased. Finally, DFT calculation revealed that surface oxygen vacancy was the adsorption and reaction site for ozone decomposition and a new mechanism of ozone decomposition in the presence of H$_2$O also was proposed. This work developed a deeper understanding to the process of ozone decomposition and would promote manganese oxide catalyst for practical application.

© 2017 Elsevier B.V. All rights reserved.

1. Introduction

Ozone with strong oxidation capacity is one of the major pollutants in the troposphere. Long-term exposed to even low level of ozone will cause various diseases including respiratory diseases and cardiovascular diseases [1,2]. The photochemical reactions involving volatile organic compounds (VOCs) and nitrogen oxides (NO$_x$) driven by sunlight was the main causes of ozone formation at the ground level [3]. Most of the electrical equipment involving discharge process [4] or irradiation of ultraviolet lamp can also induce ozone production. In recent years, thanks to the powerful oxidation capacity, ozone is widely used in air purification [5,6], water treatment [7], sterilization and disinfection [8], which leads to a serious ozone residual. Therefore, the research about ozone elimination is significant for environment protection and human health.

Because of its safety, economy and efficiency, catalytic decomposition is served as a promising and effective method for ozone removal. The active components of the catalyst are mainly noble metals (e.g. Ag [9,10], Pd [11] and Au [12]), and transition metal oxides (e.g. Mn [13], Fe [14], Cu [15], Co [16] and Ni [17]). Among all kinds of transition metal oxides, manganese oxide especially MnO$_2$ present outstanding activity [8,18]. Therefore, manganese oxide and its compound is widely researched for ozone elimination. However, the ozone removal rate is still unsatisfactory up to now, especially in wet gas flow. The latest reports [19,20] shown that the high performance for ozone elimination may be associated with its surface oxygen vacancy. Thus, a deeper understanding for ozone decomposition may contribute to develop a high performance catalyst. A generally recognized mechanism about ozone decomposition on manganese oxide has been proposed by Oyama based on the results of isotope labeling and in situ Raman spectroscopy [21]. Oyama and his coworkers deduced that the mononuclear five-oxygen coordinated species was likely the active center for ozone decomposition [22]. Xia et al. also revealed that the oxygen vacancy concentration also have significant effect on the electronic structure and catalytic performance based on the calculation results [23]. However, the direct evidence is still scarce to explain the relations between oxygen vacancy and the activity for ozone elimination. Hence, a controllable method for oxygen vacancy introduction is needed to explore the effect of oxygen vacancy.

* Corresponding authors.
E-mail addresses: zhuyf@mail.tsinghua.edu.cn (Y. Zhu), qianfan@buaa.edu.cn (Q. Zhang).

Manganese dioxide consists of various crystal phase and morphology, of which α-MnO$_2$ possesses one dimensional tunnel structure with the size of 0.46×0.46 nm [24], resulting in larger specific surface area, which is beneficial for ozone adsorption and interface reaction [19]. The tunnel structure of α-MnO$_2$ exposed more MnO$_6$ edges [25], which also is helpful for the formation of surface oxygen vacancy. A series of controllable methods to fabricate oxygen vacancies on the surface of the catalyst has been reported in our former works [26–29]. Herein, the surface oxygen vacancies were introduced on the surface of α-MnO$_2$ nanofiber via an economical and mild method, vacuum deoxidation. The concentration and extent of oxygen vacancy was tuned by changing the vacuum treatment conditions. After the surface oxygen vacancy was fabricated, the ozone removal rate at 20 h has increased from 32.6% to 95%. The effect of oxygen vacancy on the adsorption energy referring to O$_3$, O$_2$ and H$_2$O molecule was discussed based on the results of DFT calculation. Finally, we concluded that the oxygen vacancy is the active center for ozone adsorption and decomposition and a new mechanism for ozone decomposition in the wet gas flow has been proposed.

2. Experimental

2.1. Catalyst preparation

All chemicals were analytical grade and used without further purification. α-MnO$_2$ nanofiber was synthesized by a hydrothermal process. In a typical synthesis, 3.042 g MnSO$_4$·H$_2$O dissolved in 80 mL deionized water, and then 1.896 g KMnO$_4$ (Mn^{2+}:Mn^{7+} = 3:2) was added under magnetic stirring when the solution was clarified. The mixture was placed in a water bath and kept at 45 °C for 20 min. Then, the obtained suspension was transferred into a 100 mL Teflon-lined stainless steel autoclave and maintained at 150 °C for 12 h. The products were collected by centrifugation, washing with deionized water and drying at 80 °C for 10 h. The obtained power of α-MnO$_2$ was denoted as MnO$_2$. The surface oxygen vacancy was introduced by vacuum deoxidation method. A certain amount of α-MnO$_2$ power was dispersed in culture dish and then vacuum treatment was performed in vacuum oven. At the process of vacuum deoxidation, to obtain different samples, the temperature varied from 160 °C to 240 °C and the time was kept for 1, 2, 4, 6, 10 h, respectively. Then a series of oxygen vacancy α-MnO$_2$ were obtained and denoted as vac-m-nh (m = 160, 180, 200, 220, 240 °C represent the vacuum temperature, n = 1, 2, 4, 6, 10 h represent the vacuum time).

2.2. Catalyst characterization

X-ray diffraction (XRD) patterns of the powders were recorded by a Rigaku D/max-2400 X-ray diffractometer with Cu Kα ($\lambda = 1.5406$ Å) radiation at 40 kV and 40 mA. The morphology was characterized by a Field Emission Gun Scanning Electron Microscopy (FESEM, Hitachi SU-8010) and a high resolution transmission electron microscopy (HRTEM, JEM 2100F) at an accelerating voltage of 200 kV. The Raman spectra were measured on a microscopic confocal Raman spectrometer (HORIBA HR800) in the range of 100–1000 cm^{-1} for three times, and the excitation light was 514.5 nm from an Ar$^+$ laser. X-ray photoelectron spectroscopy (XPS) was measured in a PHI Quantera SXM^{TM} system and the binding energy were calibrated with the signal for adventitious carbon at 284.8 eV. Thermogravimetric analysis (TGA) was conducted on a TGA/DSC1 STARe system (METTLER TOLEDO). The samples were loaded into a pan and heated to 800 °C at a rate of 5 °C/min and the N$_2$ gas flow rate was maintained at 50 mL/min. H$_2$-TPR (tem-

perature programmed reduction) was carried out using ChemiSorb 2720 (Micromeritics).

2.3. Activity evaluation

The catalytic performance for ozone removal was evaluated in a fixed bed continuous flow quartz reactor (11 mm i.d.) at room temperature (25 °C). 100 mg catalyst was filled in the quartz tube and the space velocity was about 1.26×10^5 h^{-1}. Ozone was generated using ozonator (model 1000BT-12, Shanghai Enaly Mechanical and Electrical Technology Company) by arc discharge in the O$_2$ flow and the ozone concentration was adjusted by tuning the voltage. The high concentration ozone mixed adequately with air in the blending tank and then flowed into the reactor. The total gas flow was kept at 900 mL/min and the inlet ozone concentration was kept at 20 ± 1 ppm. The water vapor was generated by bubbling N$_2$ into the water and the relative humidity was controlled by tuning the flow rate through the humidifier, while keeping the total flow unchanged. The ozone concentration inlet and outlet has been measured by ozone detector (model 202, 2B Technologies). Finally, the ozone removal rate was calculated via the following equation: ozone removal rate = $100\% \times (C_{in} - C_{out})/C_{in}$.

## 3. Results and discussion

3.1. Formation of surface oxygen vacancy

The morphologies and microstructures were examined by FESEM and HRTEM. Fig. 1a–c present the FESEM images of the samples obtained by hydrothermal method. The α-MnO$_2$ appears as the morphology of nanofiber with diameter of 20–40 nm and length in the range of 5–10 μm. The crystal structure was characterized by XRD and the patterns of the samples vacuum treated for different time are given in Figure S1. All the samples exhibit a pure tetragonal cryptomelane type MnO$_2$ (JCPDS No. 29-1020, space group $I4/m$, $a = b = 9.815$ Å, $c = 2.847$ Å), indicating that the samples are high purity and have no obvious change of the crystal structure after vacuum treatment [24]. Further observation (Fig. 1b and c) has shown that the nanofiber present rectangular cross section. From Fig. 1d, the α-MnO$_2$ without vacuum treatment has excellent crystallinity and displays oriented growth along the [001] direction (c axis). The inter-planar distance along the growth axis is 0.316 nm, corresponding to the (310) plane of α-MnO$_2$. High temperature is beneficial for the oxygen element escaping from the lattice and forming oxygen vacancies [30] and the point defect will cause nearby lattice distortion. A defect layer will form once the defect concentration is high enough, resulting in a blurry lattice fringe in the HRTEM images. As shown in Fig. 1e, the edge of vac-200-4h becomes disordered and the thickness of the defect layer is about 1.82 nm, suggesting the damage of the ordered lattice structure on the surface of the α-MnO$_2$ nanofiber. For vac-200-10h, the thickness of the defect layer increases to 3.33 nm and the bulk defect also occurs (Fig. 1f). We tentatively guess that the defect layer forms due to the lack of oxygen element, which will be further certified in the following.

Factor group analysis about cryptomelane-type manganese oxide indicates that $6A_g + 6B_g + 3E_g$ spectroscopic species are Raman active modes [31]. Though it is difficult to observe all predicted Raman active mode, most of the Raman shift can be detected. As shown in Fig. 2, three main peaks at 174, 570 and 633 cm^{-1} have been observed. Notably, with the extension of the vacuum treatment time, the relative intensity of the peak at 570 and 633 cm^{-1} decreases. The peaks at 570 and 633 cm^{-1} are indicative of a well-developed tetragonal structure with an interstitial space consisting of (2×2) tunnels [32]. The former peak is attributed to the Mn–O
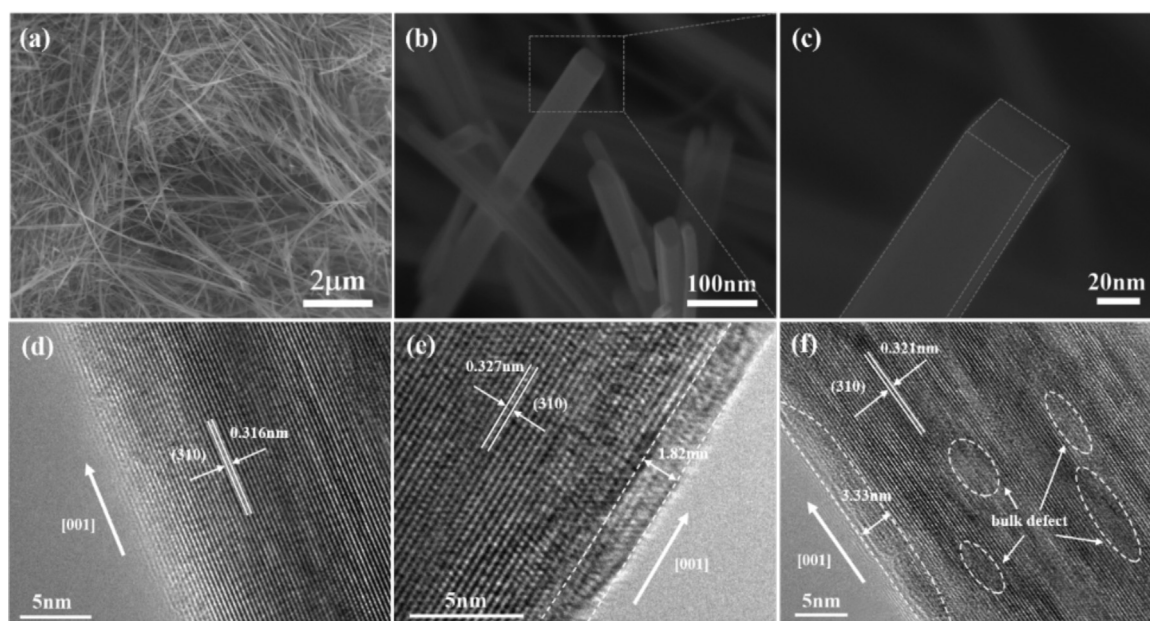
Fig. 1. FESEM images of α-MnO$_2$ nanofiber synthesized by hydrothermal method (a–c); HRTEM images of α-MnO$_2$ nanofiber vacuum treated for 0 h (d), 4 h (e), 10 h (f) at 200 °C, −0.1 MPa.
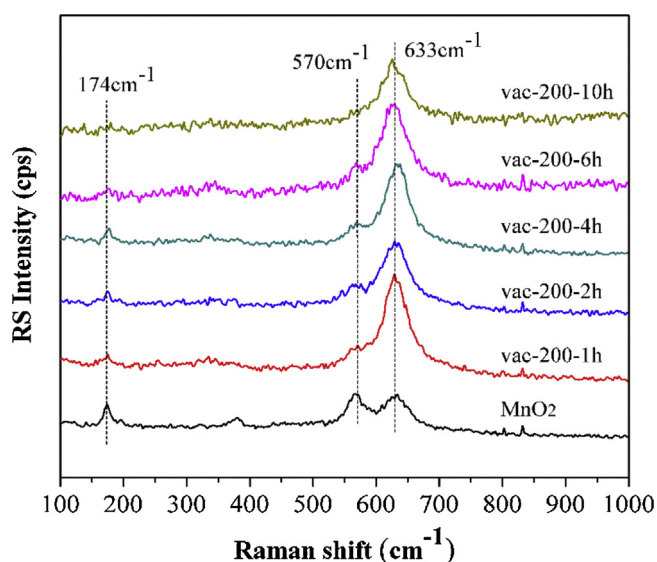
Fig. 2. Raman shift spectra of catalysts obtained by vacuum heat treatment for different time.

stretching vibration in the basal plane of the MnO$_6$ sheet, while the latter peak can be recognized as the symmetric stretching vibration of MnO$_6$ group [33]. The relative intensity of the two peaks are connected with the tunnel structure [31]. The formation of oxygen vacancy will change the spatial structure, which might be the main factor that influence the relative intensity of the peaks at 570 and 633 cm^{-1}.

The reducibility of samples has been evaluated by H$_2$-TPR experiments and the results are shown in Fig. 3a. All the samples change into green color after H$_2$-TPR experiments that indicates the catalysts are reduced to MnO. In the H$_2$-TPR profiles of α-MnO$_2$, two reduction peaks overlap and form a broad peak, centered at 315 °C. Similar finding has been previously reported and the reduction peaks may attribute to the reduction of MnO$_2$ to MnO with Mn$_2$O$_3$ and Mn$_3$O$_4$ as the intermediates [34]. For vac-200-4h, the reduction peak shift to 333 °C from 315 °C, suggesting that the Mn-O

bands become stronger after vacuum treatment [35]. And the peak will shift to 354 °C if the vacuum treatment is maintained for 10 h. The amount of H$_2$ consumption is indicative of oxygen content in the crystal and has been quantified by a standard silver oxide sample. As shown in Table S1, the theoretical H$_2$ consumption for reduction MnO$_2$ to MnO is 11.5021 mmol/g which is slightly higher than the experimental result (10.3419 mmol/g) due to the oxygen vacancy formed in the hydrothermal process [19]. More importantly, the H$_2$ consumption of vac-200-4h and vac-200-10 h reduce to 8.8470 mmol/g and 8.0870 mmol/g respectively, suggesting that the defect existing in Fig. 1e and f belongs to oxygen vacancy and the content of oxygen vacancy increases with the enhancement of vacuum treat temperature.

To further understand the deoxidation process, temperature-programmed deoxidation (O$_2$-TPD) has been performed and the results are shown in Fig. 3b. The O$_2$-TPD process of α-MnO$_2$ can be divided into four sections including low temperature (<350 °C), medium temperature (350–650 °C) and high temperature (>650 °C). And the evolution of lattice oxygen starts at 200 °C and continues above 650 °C. The peak lower at 200 °C attributes to desorption of physical adsorption water. The peak occurred between 200 °C and 350 °C is assigned as the release of chemisorbed oxygen molecule and surface lattice oxygen in the form of O$_2$ molecule [30]. The peak shift to higher temperature and the peak area also increases with the extension of the vacuum treatment time. For the samples before and after vacuum treatment, the ratio of chemisorbed oxygen on the α-MnO$_2$ surface has not changed distinctly, as proved by the following XPS results, suggesting that the peak mainly contributes to the removal of the surface lattice oxygen [36]. The increase of the peak area indicates that more oxygen can be removed at this temperature range due to the lopsided force in the distorted structure. When the temperature rises from 350 °C to 650 °C, the lattice oxygen close to the surface gradually escapes from the original site [30]. And the crystalline phase transition of vac-200-4h has been confirmed and the results are shown in Figure S2. When the temperature rises to 450 °C, vac-200-4h keeps the structure of α-MnO$_2$ but the crystalline phase of α-MnO$_2$ and Mn$_2$O$_3$ (JCPDS No. 06-0504) coexist in the structure while the temperature rises to 650 °C, indicating that crystalline phase of the out layer has transformed. For MnO$_2$, an overlapping
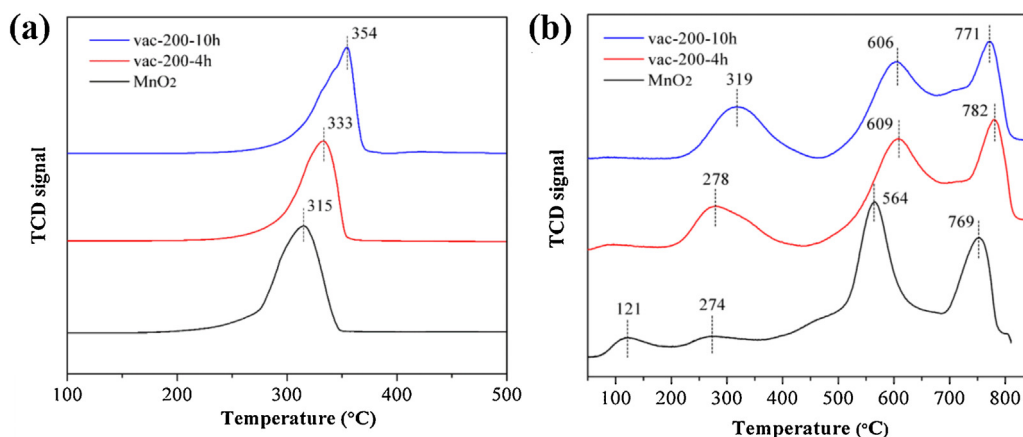
Fig. 3. H_2-TPR (a) and O_2-TPD (b) profiles of three different sample (MnO_2, vac-200-4h, vac-200-10h).

peak can be found at this temperature range, whereas the weak peak at 400–500 °C gradually disappears after vacuum treatment. Here, we infer that the weak peak corresponds to the superficial lattice oxygen removal. The peak areas at 350–650 °C also shows that the vacuum treatment reduced the oxygen content, corresponding to the results of H_2-TPR and TGA (Figure S3), suggesting that the content of oxygen vacancy can be tuned via vacuum treatment.

Considering the fact that the activity of the catalyst mainly depends on the Mn-O bond, the surface Mn state and oxygen species were analyzed via XPS. Mn 2p, Mn 3s, O1s and K signals can be observed in the full XPS spectra of all the samples (Figure S4), where K element exists as K^+ to stabilize the (2×2) tunnels structure [31]. As shown in Fig. 4a and b, the Mn $2p_{3/2}$ peak can be deconvoluted into two peaks with the binding energy at 641.9 and 642.9 eV, corresponding to Mn^{3+} and Mn^{4+} respectively [36,37], whose molar ratio is summarized in Table S2. Vac-200-4h shows the highest Mn^{3+}/Mn^{4+} molar ratio (0.62), whereas the ratio only keeps at 0.16 before vacuum treatment, suggesting that the vacuum treatment leads to more oxygen vacancy forming on the surface of α-MnO_2 nanofiber [38]. The surface average oxidation state (AOS) of Mn was estimated based on the formula[36]: $AOS = 8.956 - 1.126\Delta E_s$, where ΔE_s represents the binding energy difference between two Mn 3s peaks (Fig. 4c). Similar to the results of Mn $2p_{3/2}$, the AOS of Mn decreases from 3.84 to 3.61 after vacuum treatment, which corresponds to the H_2-TPR result. Therefore, it can be concluded that the amount of oxygen vacancy has been enhanced factually via vacuum treatment.

The oxygen species on the surface of the catalyst is important for the activity. Due to the different chemical state, the species can be distinguished via O 1s peak shown in Fig. 4 d. The asymmetrical O 1s peak can be deconvoluted into two peaks: the peak with lower bonding energy of 529.84–530.09 eV is assigned as the lattice oxygen (O1) and another with higher bonding energy of 531.36–532.21 eV is assigned as the surface adsorbed oxygen (O2) [19]. The ratios of O1/O2 have no prominent difference before and after vacuum treatment, indicating that the ratio of adsorbed oxygen has no increase. Combined with the above results of O_2-TPD, it can be drawn that more lattice oxygen near the surface is easier to release results from the lopsided force in the distorted structure after the oxygen vacancy is formed. What's more, the reactive oxygen intermediates with long chemical lifetime [39] will accumulate and occupy the oxygen vacancy. And these intermediate oxygen species may transform into lattice oxygen, which contribute to the increase of the ratio of O1/O2 from 0.3 to 0.57 and the AOS of Mn from 3.61 to 3.83 after the catalyst vac-200-4h is treated with ozone.

3.2. Adsorption energy of oxygen vacancy

To further understand the formation of the oxygen vacancy and its effect on ozone decomposition, the first-principle calculation was carried out using VASP program, based on density-functional theory (DFT). The specific calculation method is described in the Supporting Information. The cell parameters calculated through DFT + U are listed in Table S3 and the errors are lower than 0.1%, comparing with the experimental results. As shown in Table S4, the (110) plane has the lowest surface energy, whereas the planes growth along [001] direction generally possess higher surface energy, corresponding to the result reported by David et al. [40], indicating that the crystal will grow preferentially in the [001] direction and (110) plane will dominate the largest surface area according to Wulff construction theory, which is also consistent with the experimental results in Fig. 1. In the structure of α-MnO_2, each oxygen atom is coordinated to three manganese atoms, half of the oxygen atoms have an sp^2 hybridization [O (sp^2)] and lie roughly in the same plane as the three nearest Mn neighbors, while the other half have an sp^3 hybridization [O (sp^3)], lie out of the plane of the three nearest neighbors (see Table S5) [41]. Furthermore, with the predicted PBE + U oxygen vacancy formation energy on the surface of α-MnO_2 in Table S5, it also can be drawn that the oxygen vacancy is easier to form at sp^3 oxygen site compared with sp^2, owing to the lower vacancy formation energy. So, in conclusion, the surface oxygen vacancy preferentially forms at sp^3 oxygen site of (110) plane and the process is described in Fig. 5b .

Based on the results, the adsorption energy of O_2, O_3 and H_2O molecules on the catalyst surface is calculated and the results are shown in Fig. 5a, where a lower adsorption energy means a stronger adsorption. On the perfect (110) plane, the adsorption energy of O_2, O_3 and H_2O are −0.7129, −0.4448 and −0.5877 eV respectively, indicating the perfect (110) plane is negative for ozone adsorption. However, the adsorption energy of ozone significantly decreases to −3.3595 eV after the oxygen vacancy forms on the surface of (110) plane. At the same time, the adsorption energy of O_2 increases from −0.7129 to −0.6946 eV, confirming that oxygen vacancy is beneficial for the adsorption of reactant and the release of the product. The adsorption of ozone molecule before and after relaxation has been described in Fig. 5c: when an ozone molecule is introduced on the surface of oxygen vacancy (110) plane, one oxygen atom of ozone would fill into the oxygen vacancy and the rest part of ozone would be released as an O_2 molecule simultaneously. It is also shown in Fig. 5a that the adsorption energy of H_2O reduces from −0.5877 to −0.8746 eV due to the formation of surface oxygen vacancy, which means that competitive adsorption still exists in the wet gas flow. Though ozone molecule would dominate the
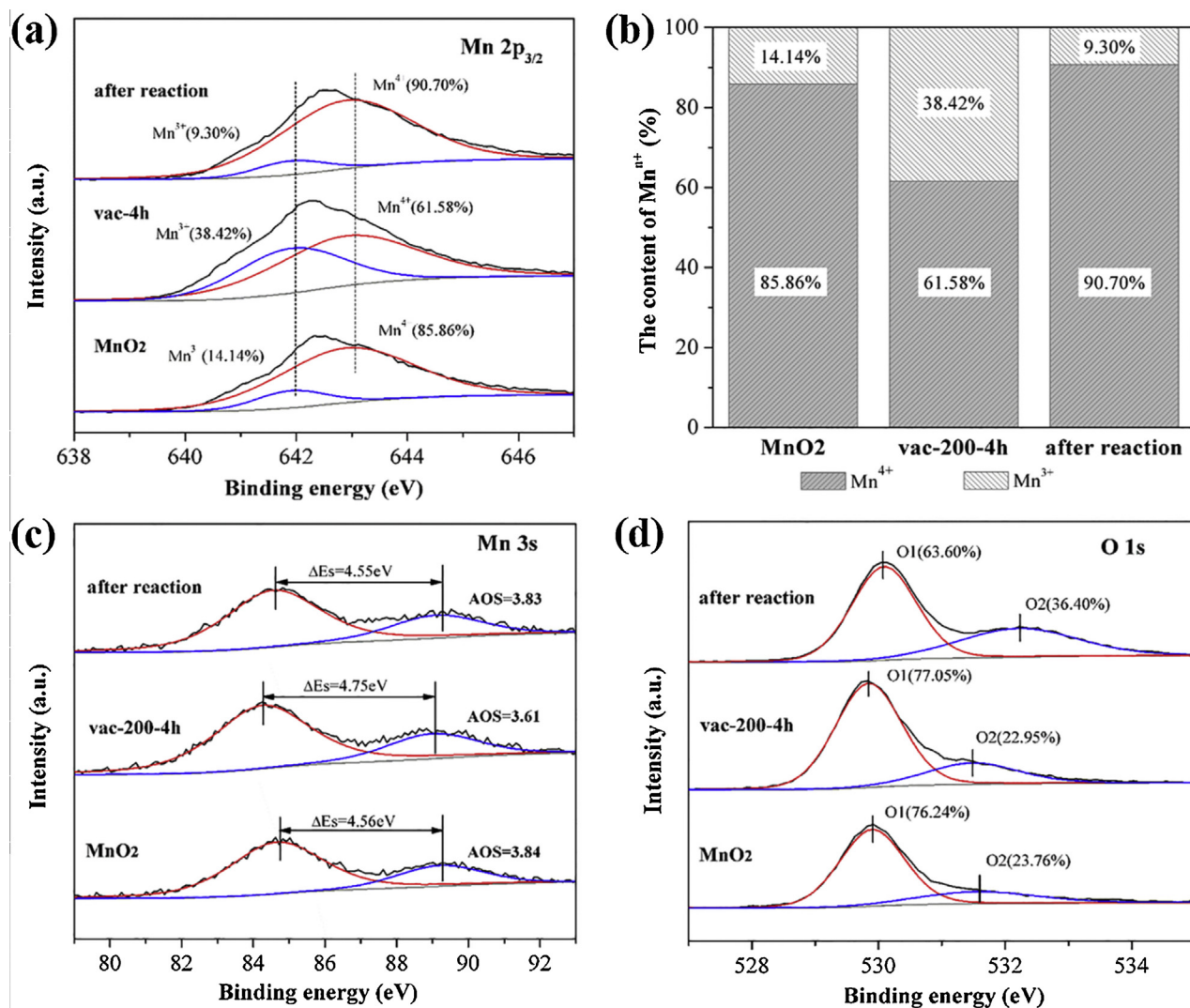
Fig. 4. High-resolution XPS spectra of MnO_2, vac-200-4h and vac-200-4h after treated with ozone at room temperature for 30 h: (a) Mn $2p_{3/2}$, (b) the content of Mn^{n+}, (c) Mn 3s and (d) O1s.
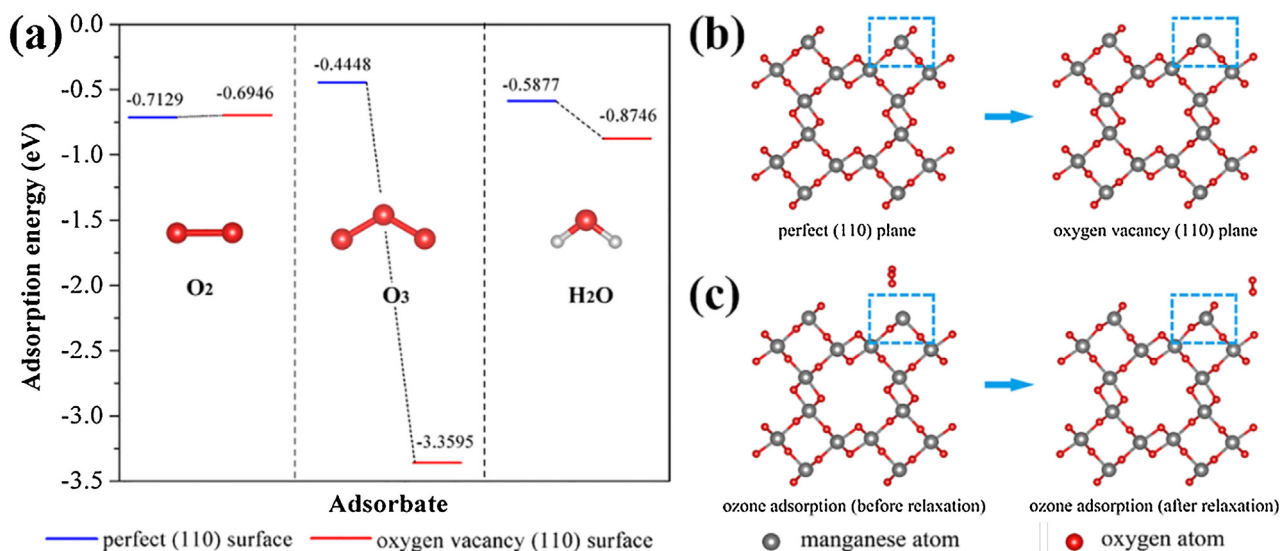

Fig. 5. (a) The calculation results of adsorption energy on the perfect and oxygen vacancy (110) surface. The process of the oxygen vacancy formation (b) and the adsorption of ozone on the (110) plane (c).

adsorption process, the competitive adsorption of H_2O molecule can not be ignored, because the adsorbed H_2O molecule is hard to desorption and would accumulate, resulting in a reduced ozone removal rate.

3.3. Performance of ozone removal

Vacuum treatment is a typical method to enhance the concentration of surface oxygen vacancy. The ozone removal rate (RH < 5%) of the samples treated in different temperature is shown in Fig. 6a . For α-MnO_2, the ozone removal rate decrease gradually and only 33% ozone molecule can be removed at 20 h, whereas it can reach at 58% after α-MnO_2 treated at 160 °C for 4 h, suggesting that the activity can be enhanced via fabricating oxygen vacancy on the surface of α-MnO_2. The results in Figure S5a also has confirmed that the enhancement of ozone removal rate is induced by oxygen vacancy rather than the effect of heat treatment by comparing the activity of the samples obtained via vacuum treatment and heat treatment at normal pressure. As shown in Figure S6, it can be found that the peak at 633 cm^{-1} becomes higher and narrower after heat treatment at normal pressure, while the change is ignorable after vacuum treatment. Therefore, we infer that the positive effect of heat treatment at normal pressure results from the increment of the crystallization degree. As can be seen in Fig. 6a, while continuing to enhance the vacuum treatment temperature, the catalyst leads to an initial increase and a subsequent decrease for ozone removal. The similar results also can be obtained in Fig. 6b from the samples vacuum treated for different time, indicating that the activity for ozone decomposition is related to the extent of oxygen vacancy, which is the same as the former reports [42]. High temperature is beneficial for oxygen atom escaping from the lattice, but the bulk oxygen vacancy will form and make an effect on the framework of the crystal if the temperature is too high or the treatment time is too long. The formation of bulk oxygen vacancy will make an influence on the framework of α-MnO_2, which is important for the catalytic process. Besides, the formation of bulk oxygen vacancy also means that the surface oxygen vacancy is excessive and the surface crystal structure and charge distribution may be changed seriously, which is not beneficial for ozone decomposition. When the treatment temperature keeps at 200 °C for 4 h, the obtain sample has possessed high concentration oxygen vacancy and the bulk defect also not formed, resulting in the highest ozone removal rate. It indicates that appropriate oxygen vacancy can enhance the performance of ozone decomposition, but the ozone decomposition would slower if the oxygen vacancy is excessive. It is shown in Figure S5b that the oxygen vacancy α-MnO_2 has well stability and the ozone removal rate could also keep at 88% after the reaction maintained for 45 h. Based on the results above, it can be concluded that the activity for ozone decomposition on α-MnO_2 nanofiber can be greatly improved by introducing appropriate oxygen vacancy.

As the reports in the literature, the catalyst is easy to deactivate in the presence of water vapor [20,43]. From Fig. 6c, we can see that the ozone removal rate at 12 h decreased from 97% to 48%, while the relative humidity (RH) increases from <5% to 30%. As the RH continues to rising, the ozone removal rate decreases gradually, suggesting that the competitive adsorption of H_2O molecule leads to an inhibition of the ozone uptake on the catalyst [18], corresponding to the calculation results. However, the deactivation is not permanent and the activity would recover once the humidity decreases. As shown in Fig. 6d, the ozone removal rate was evaluated at alternate humidity conditions. When the catalyst was firstly placed in the wet gas flow (ozone concentration was kept at 20 ppm), the ozone removal rate gradually reduces due to the competitive adsorption effect. Whereas, the ozone removal rate recovers to 100% quickly only if the RH of the gas flow is reduced. Most importantly, once the RH recovers to 50%, the ozone removal

rate also reduces to the level of the latest cycle quickly, indicating that the effect of water vapor is accumulated and not decrease after treated in dry gas flow. As we all known, ozone also has been introduced in aqueous solution to remove the organic pollutant [7,44–47], In aqueous solution, hydroxyl radical ($^{\bullet}OH$) will produce, resulting in higher removal rate of organic pollutant. Therefore, a new mechanism may occur in the process of ozone decomposition when H_2O molecule exist.

3.4. Mechanism of ozone decomposition

The literature [21] has proposed the ozone decomposition steps. However, the active site for ozone decomposition on the MnO_2 surface is still unknown. Herein, the activity for ozone decomposition was greatly improved by introducing the high concentration oxygen vacancy on the surface of α-MnO_2 nanofiber. The DFT calculation points out that oxygen vacancy is beneficial for ozone adsorption and decomposition on the catalyst surface. After the surface oxygen vacancy formed, the oxygen coordination number around Manganese site would reduce from six to five, where the mononuclear five-oxygen coordinated Manganese site is regarded as the active center of ozone decomposition [22]. Therefore, it can be concluded that the surface oxygen vacancy is the active center for ozone adsorption and decomposition. A deeper mechanism referring to the active site for ozone decomposition also has been illustrated in Scheme 1. Firstly, the dissociative ozone molecule is adsorbed on the oxygen vacancy position of catalyst (state 2) to form an oxygen molecule and leave oxygen species (O^{2-}, state 3) by electron transfer effect [22,47]. Then, the active oxygen species O^{2-} can react with another ozone molecule to form peroxide species (O_2^{2-}, state 5). Finally, the peroxide species (O_2^{2-}) will reduce to oxygen (O_2) by a metal production process and the oxygen vacancy will be released. The intermediate oxygen species O_2^{2-} also has been detected by in situ Raman [19,21].

When H_2O molecule is introduced into the reaction system, another pathway for zone decomposition may exist as shown in Scheme 2. Because of competitive adsorption, the surface oxygen vacancy will be occupied and forms suface-OH_2^+. Under the effect of electrostatic forces and hydrogen bonding, a six-membered ring will form (state 2) [44], which is unstable and will transform into surface hydroxyl group (state 3) with the release of $HO_3^{\bullet}$. Simultaneously, the surface hydroxyl group will react with ozone molecule and forms a five-membered ring (state 4). The five-membered ring will transform to surface hydroperoxyl anion (HO_2^-) with the release of O_2. The surface HO_2^- react further with ozone molecule to form $^{\bullet}O_2^-$. Finally, the $^{\bullet}O_2^-$ will be released as an oxygen molecule from the surface to achieve the regeneration of surface oxygen vacancy. However, the surface hydroxyl group has stronger interaction with H_2O molecule. If the RH is too high, water adsorption will increases, leading to block of surface active site. Therefore, the reason why the ozone removal rate has no decrease when the RH varies from 50% to <5% can be explained as the acceleration effect resulting from the new pathway for ozone elimination. The adsorbed H_2O molecule is hard to desorb from the surface oxygen vacancy, resulting in the quick decrease of ozone removal rate after the RH enhanced to 50% again.

4. Conclusion

α-MnO_2 nanofiber with high concentration of surface oxygen vacancy was obtained via vacuum deoxidation method. The amount of surface oxygen vacancy can be controlled effectively by tuning the temperature and time of vacuum treatment. DFT calculation has shown that the surface oxygen preferentially forms at sp^3 oxygen site of (110) plane. The formation of surface oxygen
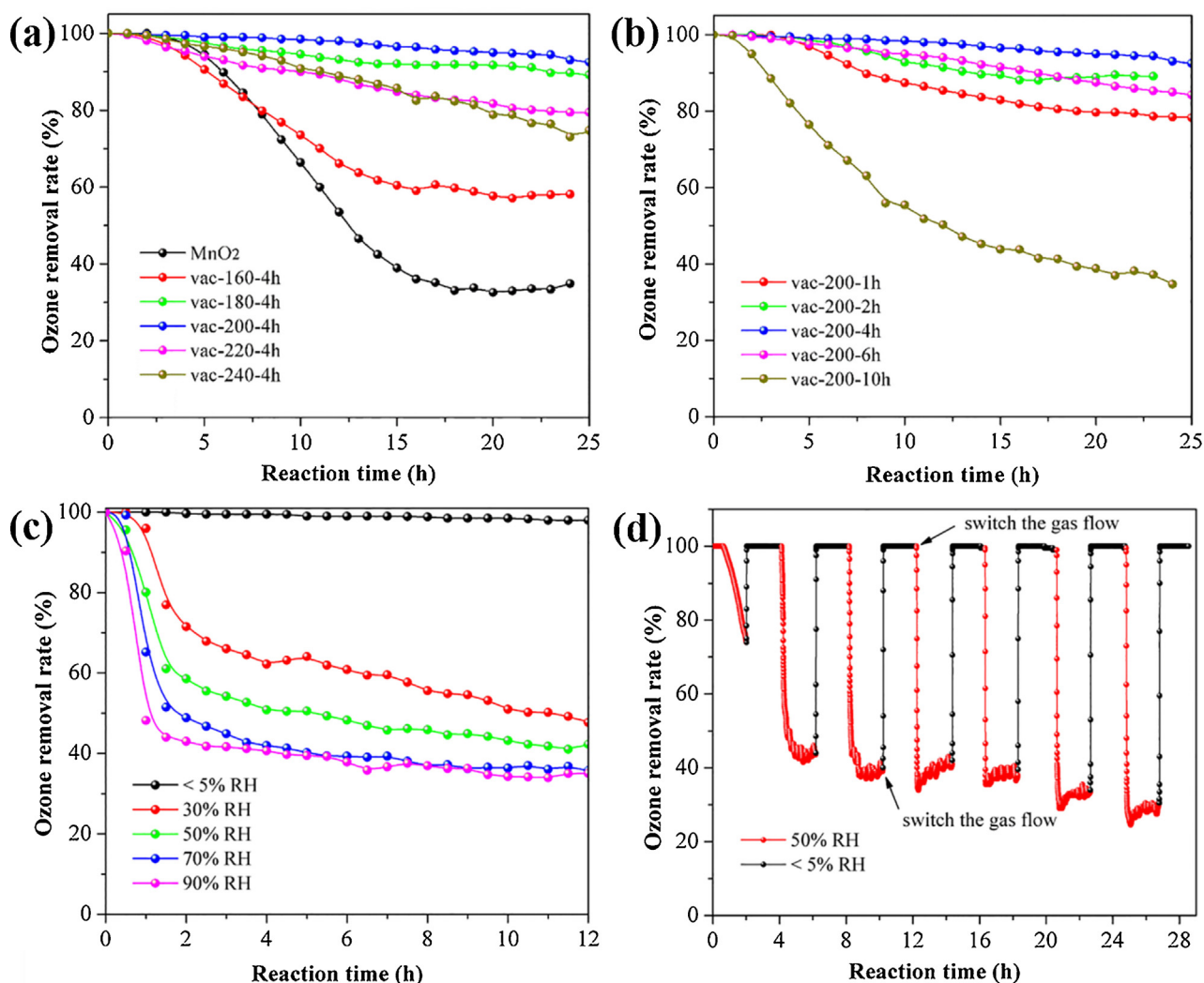
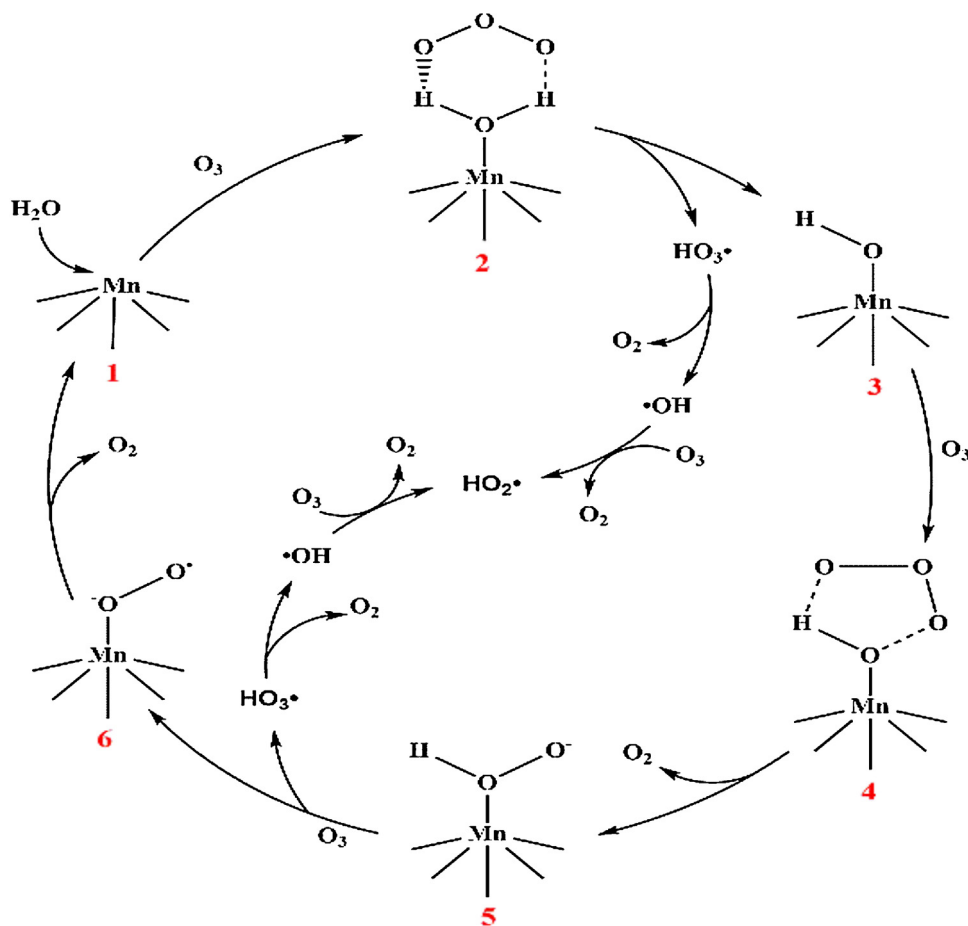**Fig. 6.** Ozone removal rate on the α-MnO₂ nanofiber vacuum treated (a) at different temperature and (b) for different time (the relative humidity of the gas flows was below 5%, 25 °C). (c) Ozone removal rate on vac-200-4h at different RH (25 °C). (d) Ozone removal rate on vac-200-4h at alternate humidity conditions (25 °C).
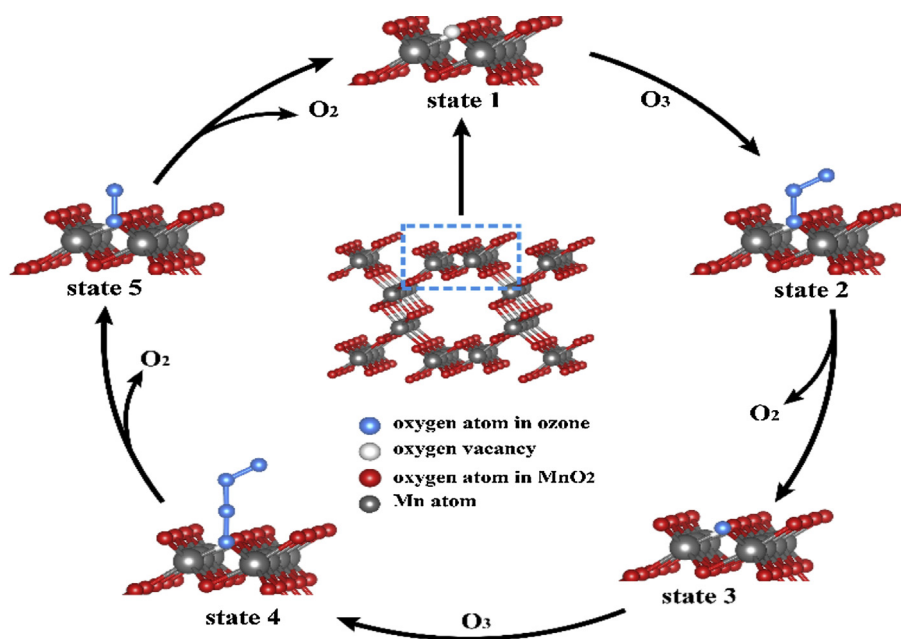
Scheme 1. The mechanism of ozone decomposition in the dry gas flow.

Scheme 2. The mechanism of ozone decomposition in the wet gas flow.

vacancy would largely improve the adsorption and decomposition of ozone molecule on the surface of α-MnO_2, resulting in that ozone removal rate at 20 h increased from 32.6% to 95%. The huge difference of ozone adsorption energy before and after oxygen vacancy forms indicates that the surface oxygen vacancy is likely to be the active site for ozone decomposition.

The experimental data also has shown that the deactivation caused by water vapor is temporary and the activity would recover once the humidity has decreased. We conclude that a new pathway for ozone decomposition in wet gas flow may exist and a new mechanism also has been proposed. Thus, a device with high performance for ozone decomposition even in high humidity can be obtained by adding a dehumidifier before the reactor. Most importantly, we just need to replace the desiccant, then the deactivated catalyst would restore its performance, which is significant for practical application.

Appendix A. Supplementary data

Supplementary data associated with this article can be found, in the online version, at http://dx.doi.org/10.1016/j.apcatb.2017.02.068.

References

[1] B. Hoffmann, H. Luttmann-Gibson, A. Cohen, A. Zanobetti, C. de Souza, C. Foley, H.H. Suh, B.A. Coull, J. Schwartz, M. Mittleman, P. Stone, E. Horton, D.R. Gold, Environ. Health Persp. 120 (2012) 241–246.
[2] J.D. Berman, N. Fann, J.W. Hollingsworth, K.E. Pinkelton, W.N. Rom, A.M. Szema, P.N. Breysse, R.H. White, F.C. Curriero, Environ. Health Persp. 120 (2012) 1404–1410.
[3] O.R. Cooper, D.D. Parrish, A. Stohl, M. Trainer, P. Nedelec, V. Thouret, J.P. Cammas, S.J. Oltmans, B.J. Johnson, D. Tarasick, T. Leblanc, I.S. McDermid, D. Jaffe, R. Gao, J. Stith, T. Ryerson, K. Aikin, T. Campos, A. Weinheimer, M.A. Avery, Nature 463 (2010) 344–348.
[4] H. Destaillats, R.L. Maddalena, B.C. Singer, A.T. Hodgson, T.E. McKone, Atmos. Environ. 42 (2008) 1371–1388.
[5] F. Lin, Z. Wang, Q. Ma, Y. Yang, R. Whiddon, Y. Zhu, K. Cen, Appl. Catal. B: Environ. 198 (2016) 100–111.
[6] M.B. Mitchell, V.N. Sheinker, W.W. Cox, K. Hardcastle, J. Phys. Chem. C 115 (2011) 11514–11524.
[7] L. Yang, C. Hu, Y. Nie, J. Qu, Environ. Sci. Technol. 43 (2009) 2525–2529.
[8] B. Dhandapani, S.T. Oyama, Appl. Catal. B: Environ. 11 (1997) 129–166.
[9] T. Batakliev, G. Tyuliev, V. Georgiev, M. Anachkov, A. Eliyas, S. Rakovsky, Ozone Sci. Eng. 37 (2015) 216–220.
[10] P. Nikolov, K. Genov, P. Konova, K. Milenova, T. Batakliev, V. Georgiev, N. Kumar, D.K. Sarker, D. Pishev, S. Rakovsky, J. Hazard. Mater. 184 (2010) 16–19.
[11] Q. Yu, H. Pan, M. Zhao, Z. Liu, J. Wang, Y. Chen, M. Gong, J. Hazard. Mater. 172 (2009) 631–634.
[12] Z. Hao, D. Cheng, Y. Guo, Y. Liang, Appl. Catal. B: Environ. 33 (2001) 217–222.
[13] C. Jiang, P. Zhang, B. Zhang, J. Li, M. Wang, Ozone Sci. Eng. 35 (2013) 308–315.
[14] Z. Lian, J. Ma, H. He, Catal. Commun. 59 (2015) 156–160.
[15] I. Spasova, P. Nikolov, D. Mehandjiev, Ozone Sci. Eng. 29 (2007) 41–45.

[16] W.-X. Tang, H.-D. Liu, X.-F. Wu, Y.-F. Chen, Ozone Sci. Eng. 36 (2014) 502–512.
[17] D. Mehandjiev, A. Naydenov, G. Ivanov, Appl. Catal. A: Gen. 206 (2001) 13–18.
[18] H. Chen, C.O. Stanier, M.A. Young, V.H. Grassian, J. Phys. Chem. A 115 (2011) 11979–11987.
[19] J. Jia, P. Zhang, L. Chen, Appl. Catal. B: Environ. 189 (2016) 210–218.
[20] C. Wang, J. Ma, F. Liu, H. He, R. Zhang, J. Phys. Chem. C 119 (2015) 23119–23126.
[21] W. Li, G.V. Gibbs, S.T. Oyama, J. Am. Chem. Soc. 120 (1998) 9041–9046.
[22] R. Radhakrishnan, S.T. Oyama, J.G. Chen, K. Asakura, J. Phys. Chem. B 105 (2001) 4245–4253.
[23] L. Li, X. Feng, Y. Nie, S. Chen, F. Shi, K. Xiong, W. Ding, X. Qi, J. Hu, Z. Wei, L.-J. Wan, M. Xia, ACS Catal. 5 (2015) 4825–4832.
[24] Y. Meng, W. Song, H. Huang, Z. Ren, S.-Y. Chen, S.L. Suib, J. Am. Chem. Soc. 136 (2014) 11452–11464.
[25] E. Saputra, S. Muhammad, H. Sun, H.M. Ang, M.O. Tadé, S. Wang, Environ. Sci. Technol. 47 (2013) 5882–5887.
[26] D. Chen, Z. Wang, T. Ren, H. Ding, W. Yao, R. Zong, Y. Zhu, J. Phys. Chem. C 118 (2014) 15300–15307.
[27] Y. Lv, Y. Liu, Y. Zhu, Y. Zhu, J. Mater. Chem. A 2 (2014) 1174–1182.
[28] Y. Lv, C. Pan, X. Ma, R. Zong, X. Bai, Y. Zhu, Appl. Catal. B: Environ. 138–139 (2013) 26–32.
[29] Z. Wei, Y. Liu, J. Wang, R. Zong, W. Yao, J. Wang, Y. Zhu, Nanoscale 7 (2015) 13943–13950.
[30] J. Luo, Q. Zhang, J. Garcia-Martinez, S.L. Suib, J. Am. Chem. Soc. 130 (2008) 3198–3207.
[31] T. Gao, H. Fjellvåg, P. Norby, Anal. Chim. Acta 648 (2009) 235–239.
[32] T. Gao, M. Glerup, F. Krumeich, R. Nesper, H. Fjellvåg, P. Norby, J. Phys. Chem. C 112 (2008) 13134–13140.
[33] S.-B. Ma, K.-Y. Ahn, E.-S. Lee, K.-H. Oh, K.-B. Kim, Carbon 45 (2007) 375–382.
[34] S. Liang, F. Teng, G. Bulgan, R. Zong, Y. Zhu, J. Phys. Chem. C 112 (2008) 5307–5315.
[35] B. Zhao, R. Ran, X. Wu, D. Weng, Appl. Catal. A: Gen. 514 (2016) 24–34.
[36] Y. Yang, J. Huang, S. Wang, S. Deng, B. Wang, G. Yu, Appl. Catal. B: Environ. 142–143 (2013) 568–578.
[37] F. Shi, F. Wang, H. Dai, J. Dai, J. Deng, Y. Liu, G. Bai, K. Ji, C.T. Au, Appl. Catal. A: Gen. 433–434 (2012) 206–213.
[38] F. Wang, H. Dai, J. Deng, G. Bai, K. Ji, Y. Liu, Environ. Sci. Technol. 46 (2012) 4034–4041.
[39] M. Shiraiwa, Y. Sosedova, A. Rouvière, H. Yang, Y. Zhang, J.P.D. Abbatt, M. Ammann, U. Pöschl, Nat. Chem. 3 (2011) 291–295.
[40] D.A. Tompsett, S.C. Parker, M.S. Islam, J. Mater. Chem. A 2 (2014) 15509–15518.
[41] C. Wang, L. Sun, Q. Cao, B. Hu, Z. Huang, X. Tang, Appl. Catal. B: Environ. 101 (2011) 598–605.
[42] Y. Lv, Y. Zhu, Y. Zhu, J. Phys. Chem. C 117 (2013) 18520–18528.
[43] M.-C. Wu, N.A. Kelly, Appl. Catal. B: Environ. 18 (1998) 93–104.
[44] L. Zhao, Z. Sun, J. Ma, Environ. Sci. Technol. 43 (2009) 4157–4163.
[45] L. Zhao, J. Ma, Z. Sun, H. Liu, Appl. Catal. B: Environ. 89 (2009) 326–334.
[46] T. Zhang, J. Ma, J. Mol. Catal. A: Chem. 279 (2008) 82–89.
[47] M. Setvín, U. Aschauer, P. Scheiber, Y.-F. Li, W. Hou, M. Schmid, A. Selloni, U. Diebold, Science 341 (2013) 988.